Rapid #: -20189264

CROSS REF ID: **2149019**

LENDER: **AZN :: Ejournals**

BORROWER: **WAU :: Suzzallo Library**

TYPE:	Article CC:CCG
JOURNAL TITLE:	Materials today chemistry
USER JOURNAL TITLE:	Materials Today Chemistry
ARTICLE TITLE:	Mn3O4 nanoparticles encapsulated in carbon cages as the electrode of dual-mechanism supercapacitors
ARTICLE AUTHOR:	Paredes Camacho, R.A.
VOLUME:	12
ISSUE:	
MONTH:	
YEAR:	2019
PAGES:	361-372
ISSN:	2468-5194
OCLC #:	

Processed by RapidX: 1/31/2023 10:17:15 AM

Materials Today Chemistry 12 (2019) 361–372

Contents lists available at ScienceDirect

Materials Today Chemistry

journal homepage: www.journals.elsevier.com/materials-today-chemistry/

Mn_3O_4 nanoparticles encapsulated in carbon cages as the electrode of dual-mechanism supercapacitors

R.A. Paredes Camacho [a], A.-M. Wu [a], S. Gao [a], X.-Z. Jin [a], G.-Z. Cao [a, b], H. Huang [a, *]

[a] Key Laboratory of Materials Modification by Laser, Ion and Electron Beams (Ministry of Education), School of Materials Science and Engineering, Dalian University of Technology, Dalian, 116024, China
[b] Department of Materials Science and Engineering, University of Washington, Seattle, 98195, WA, USA

ARTICLE INFO

Article history:
Received 21 August 2018
Received in revised form
4 April 2019
Accepted 5 April 2019
Available online 3 May 2019

Keywords:
Core-shell
Dual-mechanism
Mn_3O_4
Supercapacitors

ABSTRACT

This article reports the production of Mn_3O_4@C nanocomposites as electrodes for high-performance supercapacitor applications. A facile and low-cost synthesis method combining DC arc discharge and annealing in air at different temperatures is used. The influence of the oxidation temperatures on product microstructure and electrochemical performance is studied in detail. The Mn_3O_4@C nanocomposite obtained under 200 °C annealing owns the highest specific capacitance of 422 Fg^{-1}, with a specific energy density of 36 $Whkg^{-1}$ and excellent stability after 1000 cycles. The enhanced electrochemical response is attributed to a well-defined core-shell structure that has a defect-enriched carbon shell and pseudocapacitive Mn_3O_4 core. Carbon promotes the ion exchange with electric double-layer capacitance, while Mn_3O_4 contributes the pseudocapacitance during its faradaic redox reactions.

1. Introduction

The development of eco-friendly energy storage and conversion technologies is the key to remediate the climate change situation, where supercapacitors might be the most advantageous choice in the near future [1]. Supercapacitors are divided according to their energy storage mechanisms, i.e., by means of an electric double-layer capacitance (non-Faradaic) or by a redox pseudocapacitance (Faradaic) [2]. Carbon materials with large surface areas, a huge number of pores, and intrinsic high conductivity, like activated carbon, carbon nanotubes (CNT), and graphene, are suitable to serve as electric double-layer capacitors (EDLCs) [3]. The fast electrostatic process provides them with a noteworthy reversibility and a long-life cycling stability (>500,000 cycles), where high power densities over 10 $kWkg^{-1}$ can be achieved [4]. On the other hand, pseudocapacitors are distinguished by reversible redox reactions and adsorption of ions from the electrolyte on their surface. They provide far higher capacitance and energy density (around 1–10 $Whkg^{-1}$) than EDLCs but lack long-term stability and power density (>2 $kWkg^{-1}$) [1,2]. The most popular pseudocapacitive material is ruthenium oxide (RuO_2) because of its high specific capacitance (>1000 Fg^{-1}). However, its main drawback is its high toxicity, which is a determining factor to pursue the study of a suitable replacement [5].

In this regard, polyvalent and environmentally friendly transition metal oxides are now intensively explored, where the versatility of manganese stands out due to a variety of stable oxides and a wide diversity of crystal structures. Hausmannite (Mn_3O_4) is an important representative of manganese oxides because it has a defect chemistry, morphology, and porosity (from ultramicropores to mesopores) that play a significant role in the electrochemical properties when it is used as electrode materials [6]. In consequence, its potential application for supercapacitors has been demonstrated [7–11]. Unfortunately, two factors such as low conductivity (10^{-8} Scm^{-1}) and poor cycling stability restrict the real application of Mn_3O_4 as the electrode material [7,12,13]. Recently, many researchers focus on finding alternative ways to overcome these deficiencies by producing Mn_3O_4 nanoparticles decorated on the surface of graphene sheets. Hummers' method has been applied for the synthesis with many different strategies to attach Mn_3O_4 nanoparticles on the surface of graphene layers, such as, the modified Hummers' method with KNO_3 [7], hydrothermal reduction of β-MnOOH [8], chemical decomposition of manganese hexacyanoferrate [9], ultrasonication of MnO_2 organosol [14], etc. [10,12,13,15,16]. Furthermore, the activated carbon has also been a suitable conductive component. For instance, some composites

* Corresponding author.
E-mail address: huanghao@dlut.edu.cn (H. Huang).

https://doi.org/10.1016/j.mtchem.2019.04.003
2468-5194/

such as activated carbons-Mn_3O_4-carbon black [17] and Mn_3O_4-activated carbon [11] were characterized as electrode materials, but their capacitive performance was not completely satisfactory. All the studies mentioned previously obtained the maximum capacitance ranging from 131 to 312 Fg^{-1}, which still is not competitive enough. The best design of high-class supercapacitors is to merge the assets of carbonaceous materials and pseudocapacitive materials into one heterogeneous-structure electrode similar to a core-shell formation. This unified structure offers a higher synergistic relationship by reinforcing the electroactivities of each component [5]. Chen et al. [18] demonstrated in their study that the capacitance of MnO_2 nanoparticles dispersed on the outer surface of CNTs (790 Fg^{-1}) was outperformed by that of MnO_2 nanoparticles confined inside CNTs (1250 Fg^{-1}). Such a great difference in capacitance was attributed to the core-shell structure. Moreover, Liu et al. produced onion-like C shells using the arc discharge method. The as-produced carbon layers possessed high flexibility and electrical conductivity, which were used as matrices for Co_3O_4 [19], NiO [20], CuO [21] anodes to improve their Li-ion high-rate charge-discharge capability and cycling stability.

Herein, this article describes the production of a novel Mn_3O_4@C nanocage, through a simple, industry-scalable, and environmentally safe approach, for high-capacitive supercapacitor applications. The method consists of DC arc discharge evaporation of Mn bulk in a CH_4 ambient to produce the precursor Mn_7C_3@C nanocapsules and their posterior oxidation in air at different temperatures. Mn_7C_3@C oxidation temperature is optimized at 200 °C. The outstanding electrochemical performance and cyclability attained by Mn_3O_4@C-200 °C nanocomposite were endorsed to its ideal configuration (large deal of defects and wrinkles in the graphitic layer, sufficiently open Mn_3O_4 crystal structure) and its synergetic bonding among these electrochemically active materials, ensuring a rapid ion-exchange process within the microstructure. Accordingly, it is reasonable to affirm that this may lead to an alternative method for manufacturing new supercapacitor material.

2. Experimental section

2.1. Fabrication of Mn_7C_3@C nanoparticles

DC arc discharge plasma method has been adopted to fabricate various nanostructures such as metal-based nanoparticles [22], graphene [23], and carbon-coated nanocapsules for energy storage [24–26]. Following the same DC arc discharge methodology described in those previous works, a carbon rod was set as the cathode and Mn bulk (99.99% purity) as the anode on a water-cooled copper stage. Once the vessel compartment was vacuumed to 10^{-2} Pa, a mixture of methane (0.02 MPa) and argon (0.02 MPa) was introduced. The arc discharge was ignited at a steady current of 90 A with a voltage of about 40 V. The Mn bulk was evaporated for 15 min. The evaporated nanoparticles were deposited on the cooling chamber wall. After being passivated in air for 8 h, the Mn_7C_3@C nanoparticles were finally collected from the chamber wall.

2.2. Synthesis of manganese oxide@C nanocomposites

The following step was the annealing of Mn_7C_3@C nanoparticles that were first deposited in an alumina crucible and then placed in the central zone of the quartz tube to ensure uniformity of heat transfer. The powder was heated at a rate of 3 °C min^{-1} from room temperature (R.T.) to 200 °C and kept for 2 h at 200 °C still in air to get the sample. The same procedure was implemented at 300 and 400 °C.

2.3. Characterization

The phases of Mn_7C_3@C and Mn_3O_4@C nanopowders were confirmed by X-ray diffraction (XRD, PANalytical Empyrean) using Cu K_α radiation ($\lambda = 1.5416$ Å). Raman spectra were recorded by using an inVia spectrometer (Renishaw, England) with an excitation wavelength of 632.8 nm. Thermogravimetric analysis (TGA) and differential thermal analysis (DTA) were carried out in a DSC822/TGA/SDTA851 from 25 °C to 700 °C, with a heating rate of 10°Cmin^{-1} in oxygen. The morphology and structure analyses were performed by transmission electron microscopy (TEM) and high-resolution transmission electron microscopy (HRTEM) using an FEI Tecnai G20 S-type Twin.

2.4. Electrochemical measurements

Nickel foam is chosen as the substrate and a current collector in our work because it serves as excellent conducting backbone, and its porous structure provides excellent mechanical stability and allows easy access of electrolyte ions to electroactive surfaces via short pathways, as many other investigations have demonstrated [7,12,27–32]. Thus, to exclude its pseudocapacitive contribution, the nickel foam was sonicated in a 3 M HCl solution for 20 min. In this way, possible oxides and hydroxides were cleaned off the surface of the electric collector. After that, it was sonicated in deionized water for 10 min to wash off the acid, and then it was dried in the oven for 2 h. The working electrode preparation consisted in mixing the active material, carbon black and poly-(vinyl difluoride) in N-methyl pyrrolidone at a weight ratio of 85:10:5 until it formed a slurry paste. Then it was coated onto the Ni foam, dried in vacuum at 100 °C for 10 h, and finally pressed under a pressure of 10 MPa. The mass loading of the active material was 2 mg cm^{-2}. The electrochemical measurements were performed on the workstation CHI760e. A standard three-electrode cell was set with the active material on the nickel foam as the working electrode, Ag/AgCl as the reference electrode, Pt foil as the counter electrode, and 30% w/w KOH solution as the electrolyte. Cyclic voltammograms (CV) were performed at scan rates of 1, 5, 10, 50, 100, and 500 mVs^{-1}. CV results were calculated using the following equation: $C_s = \frac{\int I(V)dV}{2*m*\Delta V*v}$, where C_s is the specific capacitance in Fg^{-1}, I is the current in Amp, m is the mass of the entire active material in g, ΔV is the potential window in V, and v is the scan rate in Vs^{-1}. Current densities used for galvanostatic charge-discharge were 0.3, 0.5, 0.8, 1, 2, and 3 Ag^{-1}, under a potential window of −0.4 to 0.4 V. Charge-discharge results were calculated using the following equation: $C_s = \frac{I*\Delta t}{m*\Delta V}$, where Δt is the discharge time in s. Electrochemical impedance spectroscopy (EIS) measurements were carried out in a frequency range of 0.01 Hz–100 kHz, with AC amplitude of 5 mV.

3. Results and discussion

To determine the chemical composition and crystallite phases, XRD analysis is performed on the precursor, as displayed in Fig. 1(a). The curve for the nanoparticles owns main characteristic peaks at $2\theta = 39.76°$, 40.35°, 42.6°, and 44.66°, and they are indexed as the crystal planes of (015), (201), (105), and (115) in the orthorhombic Mn_7C_3 (JCPDS 01-089-6159). This strongly indicates that manganese is an active element to react with carbon. A diffraction peak around 26° is attributed to the characteristic (002) plane of graphitic carbon structure (JCPDS 001–0646). The carbon sourcing from the graphite anode and methane gas both is plenty in the chemical reaction with Mn where a mixture of C and Mn_7C_3 is attained as the final product, as it is illustrated in Mn–C phase

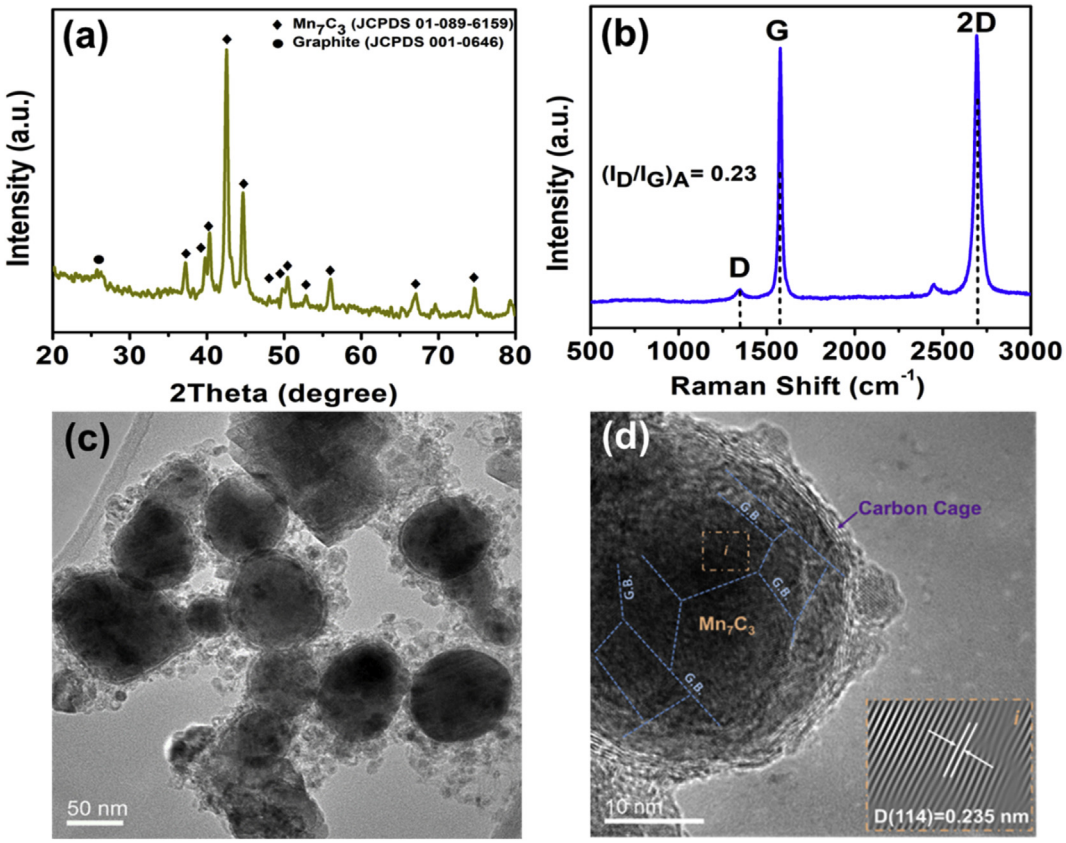

Fig. 1. Microstructural characterizations of the Mn_7C_3@C nanoparticle precursor. (a) XRD pattern, (b) Raman spectra, (c) TEM, and (d) HRTEM image with the inset showing the d-spacing of Mn_7C_3 for (114) plane. XRD, X-ray diffraction; TEM, transmission electron microscopy; HRTEM, high-resolution transmission electron microscopy.

diagram [33]. According to Scherrer's equation, $C_{size} = K\frac{\lambda}{B\cos\theta}$, where C_{size} is the apparent crystallite size in Å, K is shape factor, B is the instrument broadening in radians, θ is Bragg angle in radians, and λ is radiation wavelength; the approximate size range of the Mn_7C_3 grains was calculated to be around 26 nm [34].

Raman spectroscopy of carbons provides not only unique vibrational and crystallographic information but also unique information about physical properties that are pertinent to electrons and phonons. Therefore, to characterize the degree of graphitization, Raman spectroscopy is performed on the as-produced nanocomposite. As it can be seen in Fig. 1(b), D, G, and 2D, peaks are present in the sample's spectra around 1343.7, 1574.5, and 2692.9 cm^{-1}. The D peak arises from the disorder associated with structure defects, amorphous carbon, or edges that can break the carbon symmetry, and it can always be found in multilayer or rich-defect graphene sheets. G, a primary in-plane vibrational mode, is strictly related to the presence of six-fold aromatic rings. The other main peak is 2D, which is a second-order overtone of a different in-plane symmetric C-C stretching vibration peak D. D and 2D peak positions are dependent on the laser excitation energy, which means that they have a dispersive nature [35,36].

A Lorentzian function fitting is used to calculate the areas for the ratios I_D/I_G. At a fixed λ, I_D/I_G is a pointer to confirm the degree of graphitization or defect density in carbon materials, and increased I_D/I_G value represents more disordered structure in graphitic carbon [37]. In our research, 0.02 MPa CH_4 nanocomposite owns a low value of 0.23, which means that it possesses a high degree of graphitized carbon. These findings agree well with TEM and HRTEM images. Using the Tuinstra and Koenig's formula [38], L_a, the in-plane crystallite size, can be calculated as $\frac{I_D}{I_G} = \frac{A}{L_a^2}$, where A is a constant value of 102 nm^2 [39]. It is demonstrated that the electrical conductivity of graphitic carbons is enhanced in direct proportion with the size of the crystallite [23,40]. In our case, the L_a size was around 21.1 nm which ensures the conductivity of the carbon as an energy storage material.

The TEM morphologies of the Mn_7C_3@C precursor are shown in Fig. 1(c) and (d). Fig. 1(c) shows a conformation of spherical nanoparticles in well-dispersed distribution without visible agglomeration. The mean size of the particles is about 70 nm. A lot of tiny granules, as they are found within several nanometers, clinched together around the nanoparticles. This is a common morphology of the particles formed in the arc discharge process. The large temperature difference between the wall surface and the arc plasma stimulates spontaneous nucleation of the ionized particles, whereas the particle growth is limited due to the fast cooling condition [41]. High-resolution TEM, shown in Fig. 1(d), is conducted on the single nanoparticle, and its microstructure is clearly confirmed as core-shell configuration. The carbon shell is onion-like graphitic cage consisting 5–7 carbon layers within the thickness of 1.5 nm. A large deal of defect and mismatch of the layers can be observed, which is similar to most carbon-coated nanostructures produced by the arc discharge method [23]. Inside the carbon cage, the solid core displays the crystallized Mn_7C_3 nanosphere composed of several fine grains, whose boundaries are distinguishable, shown as the meshwork of dash lines in Fig. 1(d). The inset of Fig. 1(d) provides the inverse fast Fourier transform images of the selected rectangular region '*i*' in the nanocore. One can measure the (114) planes of Mn_7C_3 with a spacing distance of 0.235 nm. Hence, the precursor we have obtained is defined accurately as Mn_7C_3@C nanocapsules. In the succeeding process,

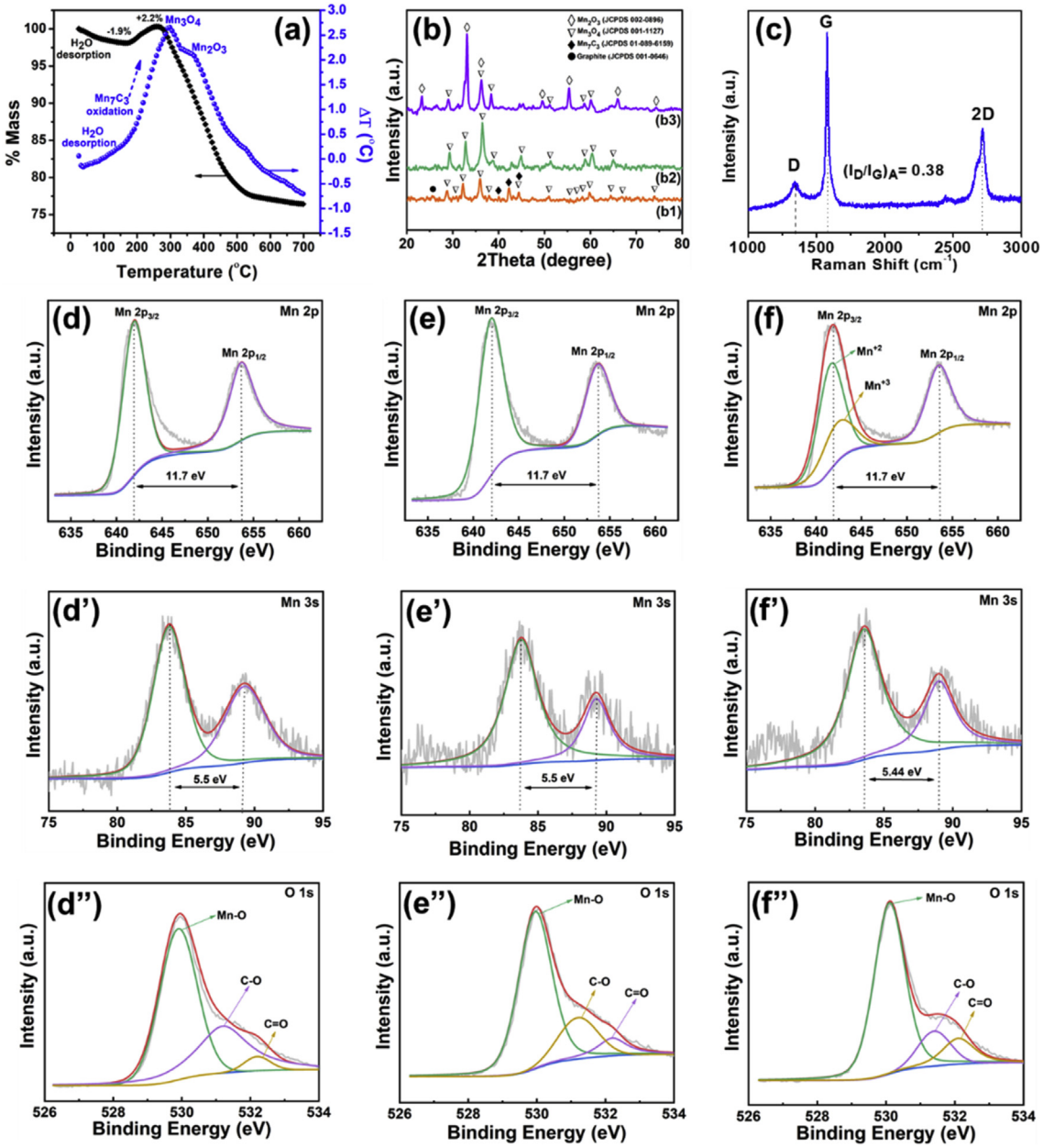

Fig. 2. (a) TGA and DTA curves for the Mn_7C_3@C nanoparticle precursor; (b) XRD patterns of (b1) MOC-200, (b2) MOC-300, and (b3) MOC-400; (c) Raman spectra of MOC-200. XPS spectra of the as-prepared nanoparticles, (d, e, and f) Mn 2p region of MOC-200, MOC-300, and MOC-400; (d', e', and f') Mn 3s region of MOC-200, MOC-300, and MOC-400; (d'', e'', and f'') O 1s region of MOC-200, MOC-300, and MOC-400. TGA, thermogravimetric analysis; DTA, differential thermal analysis; XPS, X-ray photoelectron spectroscopy.

the precursor will be oxidized in controlled temperature and progressive degree, ensuring that the Mn_7C_3 nanocore is oxidized into manganese oxide without altering the carbon cage.

To select the proper temperature of oxidation, TGA and DTA are conducted from R.T. to 700 °C in an oxygen atmosphere, the result of which is illustrated in Fig. 2(a). In the TGA curve, 3 stages can be divided at the temperature range of R.T.–176 °C, 176–262 °C, and 262–700 °C. The first stage depicts a 1.9% mass loss due to the removal of the physically and chemically bonded water [19,30]. For the second, there is a conspicuous weight increase of 2.2% (262 °C), which can be attributed to the Mn_7C_3 nanoparticles oxidation to Mn_3O_4, i.e., $3Mn_7C_3 + 14O_2 \rightarrow 7Mn_3O_4 + 9C$. The last phase witness a sharp mass loss of 22.6% until 531 °C, which can be ascribed as burning of carbon into CO_2. The oxidation terminates after 531 °C, and the mass of the sample keeps unvaried until 700 °C. As for DTA, two main exothermal peaks can be appreciated; the first belongs to the completion of the oxidation process of Mn_7C_3 to Mn_3O_4 at 297 °C, in good accordance with the weight gain from the TGA curve. There is a 75.63% mass loss corresponding to the carbon content, and 24.37% mass remained corresponding to the Mn_3O_4. Thus, this represents a mass ratio of Mn_3O_4:C = 1:3.1. The second peak belongs to the promoted oxidation of the Mn_3O_4 phase into Mn_2O_3 at 370 °C, $4Mn_3O_4 + O_2 \rightarrow 6Mn_2O_3$. As it can be confirmed, the oxidation of bulky Mn_7C_3 can be realized at least over 1300 °C [33]. The Mn_7C_3 core, as it is characterized in the HRTEM, consists of ultrafine nanograins, which store a large excess energy in the grain boundaries or as the form of in-grain defects such as dislocations. These non-equilibrium defects constitute an extra driving force and enable the oxidation to proceed at relatively low temperature. The oxidation of the Mn_7C_3@C NCs, based on the thermal analysis, is set

at the temperature of 200, 300, and 400 °C. The corresponding oxidized samples are speculated chemically as manganese oxide in carbon cage, and for the sake of convenience, they are labeled in the abbreviated form of MOC-200, MOC-300, and MOC-400 in the following discussions.

The XRD patterns of the as-annealed samples are depicted in Fig. 2(b), referring to the standard spectra from JCPDS cards. The sample MOC-200 (b1) owns main characteristic peaks at $2\theta = 28.9°$, 31.1°, 32.53°, and 36.19° corresponding to the (112), (200), (103), and (211) planes of tetragonal Mn_3O_4 hausmannite, respectively. The remains of the Mn_7C_3 peaks at $2\theta = 40.3°$, 42.6°, and 44.6° reveal an incomplete oxidation process of the core at 200 °C. MOC-300 (b2) shows the primality of the Mn_3O_4 phase. The peaks of the Mn_7C_3 fall to an inappreciable extent, indicating the Mn_7C_3 nanocores have been approaching the full-oxidated state. In the curve of MOC-400 (b3), the peaks of Mn_2O_3 phase are found coexisting with those of Mn_3O_4. This identifies the possibility of the upgraded oxidation from Mn_3O_4 to Mn_2O_3, which arrives at good agreement with the TGA-DTA results, where an exothermal peak around 370 °C is displayed for such oxidation process. The Raman spectra of MOC-200 in Fig. 2(c) indicates that the carbon structure after the oxidation process has the changes in the structure related to disorder and induced defects in the graphitic layers. This is demonstrated with an increase of I_D/I_G from 0.23 to 0.38 and the reduction of the size of L_a crystallite from 21.1 to 16.4 nm.

X-ray photoelectron spectroscopy was performed to verify the electronic states of Mn in the as-prepared MOC-200, MOC-300, and MOC-400 nanocomposites. The high resolution spectra of Mn 2p is shown in Fig. 2(d)–(f). Two characteristic peaks for Mn species arose at 641.9 and 653.63 eV for MOC-200, 641.89 and 653.63 eV for MOC-300, and 641.75 and 653.45 eV for MOC-400 attributed to Mn $2p_{3/2}$ and $2p_{1/2}$, respectively. The energy separation for all the samples was 11.7 eV, which is in accordance with previous studies [42]. The peaks for binding energy level of Mn 3s are located at 83.77 and 89.27 eV for MOC-200, 83.77 and 89.27 eV for MOC-300, and 83.56 and 89 eV for MOC-400. The energy separation of this spin orbit splitting is really important to determine the possible valence of Mn [43]. According to some references [44,45], the theoretical values for the energy separation of Mn_3O_4 and Mn_2O_3 are 5.5 and 5.4 eV, respectively. Fig. 2(d')-(f') show that there is a difference in energy separation between MOC-200 and MOC-300 ($\Delta E = 5.5$) with the one of MOC-400 ($\Delta E = 5.44$), which represents the change in the chemical state of the nanocomposite once the temperature reaches 400 °C and matches what was seen in XRD measurements (Fig. 2(b)). In agreement with theoretical values of Mn 2p and 3s spectra, the energy separation of MOC-200 and MOC-300 corresponds to Mn_3O_4. In contrast, MOC-400 owns an energy separation of 5.44 eV in Mn 3s spectra and additionally has two satellite peaks in Mn 2p spectra at 641.6 and 642.3 eV, which are related to Mn^{+2} and Mn^{+3}, respectively [46,47]. These two factors are evidence of the coexistence of Mn_3O_4 and Mn_2O_3 species in MOC-400. Finally, O 1s spectra shows (Fig. 2(d'')-(f'')) one main peak at 529.9, 529.9, and 530.1 eV for MOC-200, MOC-300, and MOC-400, respectively, which are consistent with the binding energy values for Mn–O bond found in other studies [43,48]. Two satellite peaks can be found in all the samples, which belong to C–O and C=O bonds [48].

Fig. 3(a) and (a') show the TEM and HRTEM morphologies of MOC-200, where the core-shell configuration is still maintained in the less-sintered nanoparticles. One can easily see that the carbon cage, after oxidation, is thickened to near 6 nm and preserves the large extent of the defect-rich multilayered structure. The exceeding increment of the graphitic layers is driven by the fast growth of carbon, the main product when oxygen reacts with Mn_7C_3. With the constraint of the existing carbon cage, the expelled carbon accumulates on the internal surface and physically increases the thickness. Meanwhile, the solid core experiences obvious volumetric shrinkage during the oxidation. Clear separation can be observed between the carbon cage and the oxide core in Fig. 3(a'). The core of MOC-300 exhibits a quasispherical morphology linked by 1-D carbon network (Fig. 3(b) and (b')). The core-shell structure vanishes with the exuviation of the carbon cage away from the

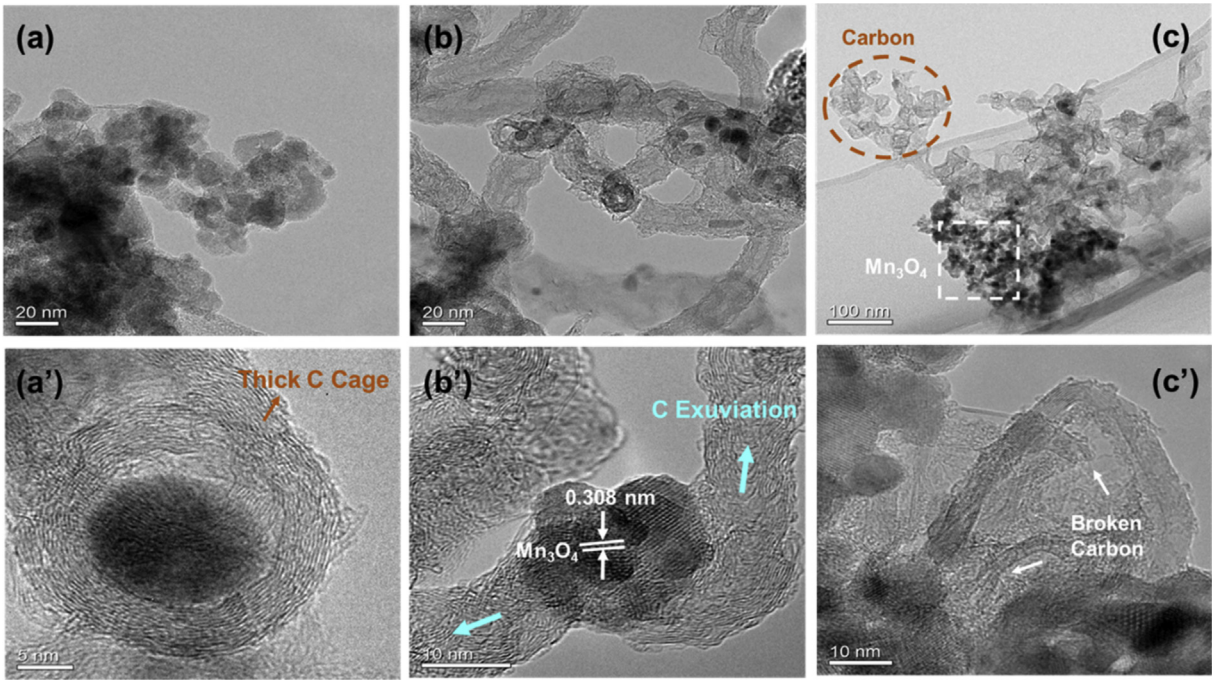

Fig. 3. Structural evolution of Mn_3O_4@C composite nanomaterials. TEM images of (a) MOC-200, (b) MOC-300, and (c) MOC-400. HRTEM images of (a') MOC-200, (b') MOC-300, and (c') MOC-400. TEM, transmission electron microscopy; HRTEM, high-resolution transmission electron microscopy.

Mn_3O_4 core, in the direction of the arrows shown in Fig. 3(b), leaving the core half exposed. Apparently, unlike the MWCNTs, which consist of parallel unidirectional carbon layers, the carbon wires are made up of piles of tiny and curved graphene segments, just as they were found previously in the carbon cages. With the help of the thermal convex during the annealing of the Mn_7C_3@C NCs, the graphene segments in the carbon cages are driven to flow in one direction, which are linked to each other by the van der Waals' force. In Fig. 3(c) and (c'), MOC-400 sample displays two disengaged set of structures, broken graphitic layers and Mn_3O_4 nanoparticles agglomerate. Thus, when the protection of carbon cages is lost, the Mn_3O_4 nanoparticles are apt to agglomerate due to the spontaneous tendency of decreasing their surface energy. The carbon, at the same time, is continuously burnt into CO_2, leading to heavy destroyed structures in pieces of fragments (Fig. 3(c')).

Scanning electron microscopy images of all the as-prepared nanoparticles are shown in Fig. 4. As it can be seen in Fig. 4(a) and (b), Mn@C precursor and MOC-200 nanoparticles preserve an isolated spherical morphology. Accordingly, the core-shell structure is intact after the oxidation at 200 °C. Furthermore, MOC-300 and MOC-400 images clearly illustrate the process of carbon disengagement from the core Mn_3O_4 after the annealing in air at 300 and 400 °C, respectively. One can easily see carbon wires on the side of the agglomerated Mn_3O_4 nanoparticles (Fig. 4(c) and (d)). These results are consistent with what was observed in the TEM images shown in Fig. 3.

The mechanism of Mn_7C_3@C nanocomposite production and its subsequent oxidation process to synthesize Mn_3O_4@C are shown in Fig. 5(a). When the electric discharge produces the flame between the carbon rod and manganese block, Mn atoms along with carbon, hydrogen, and argon atoms are evaporated into a plasma state. Constant collisions transport the atoms away from the hot zone of the arc. The cooling process happens in the large temperature gradient away from the plasma to the chamber room where all atoms are prompted to come closer to each other for the vapor-liquid-solid growth to begin [22]. This is a critical stage of the formation mechanism because unlike traditional physical deposition using the arc discharge technique [22,25], a reaction between carbon and manganese is produced right after the condensation. After the temperature reaches 1300 °C approximately, Mn_7C_3 is crystallized, and the excess carbon is precipitated. As demonstrated before, these crystals are in spherical shape, which is a sign of high surface tension of the liquid or semiliquid Mn carbide. The excessive C atoms deposit on the carbide surface to form a continuous carbon layer surrounding the spherical carbide-manganese particles. Therefore, the initial layer of carbon creates a preferential growth for the rest of the carbon layers [49]. However, this step happens so fast (due to the high-temperature gradient on the wall of the chamber) that there is no time for the upcoming layer to match perfectly with the subjacent one. On the other hand, the spherical shape of the nanoparticles induces serious bending, which breaks the continuity of the graphitic layer. In consequence, a large density of defects is formed. The as-prepared Mn_7C_3@C is annealed in air at different temperatures afterward. The core-shell structure is conserved only after the 200℃ oxidation, which owns a thicker graphitic carbon layer. This is due to a reaction of Mn carbide with oxygen, i.e., $3Mn_7C_3 + 14O_2 \xrightarrow{200^{\circ}C} 7Mn_3O_4 + 9C$, which produces carbon and Mn_3O_4. The nanocore undergoes a shrinkage after the reaction while the graphitic cage grew at the expense of this reaction.

The main features of the core-shell architecture that are essential to achieving a dual-mechanism are represented in Fig. 5(b). First, the electric double-layer capacitance achieved by the graphitic carbon satisfies all the requirements, such as high conductivity, high area, electrochemical stability, and open porosity [1,4], for the delivery of double-layer capacitance proposed by the Stern model [50]. Furthermore, its electronic conductivity provides fast charge transfer from/to the current collector (nickel foam) by

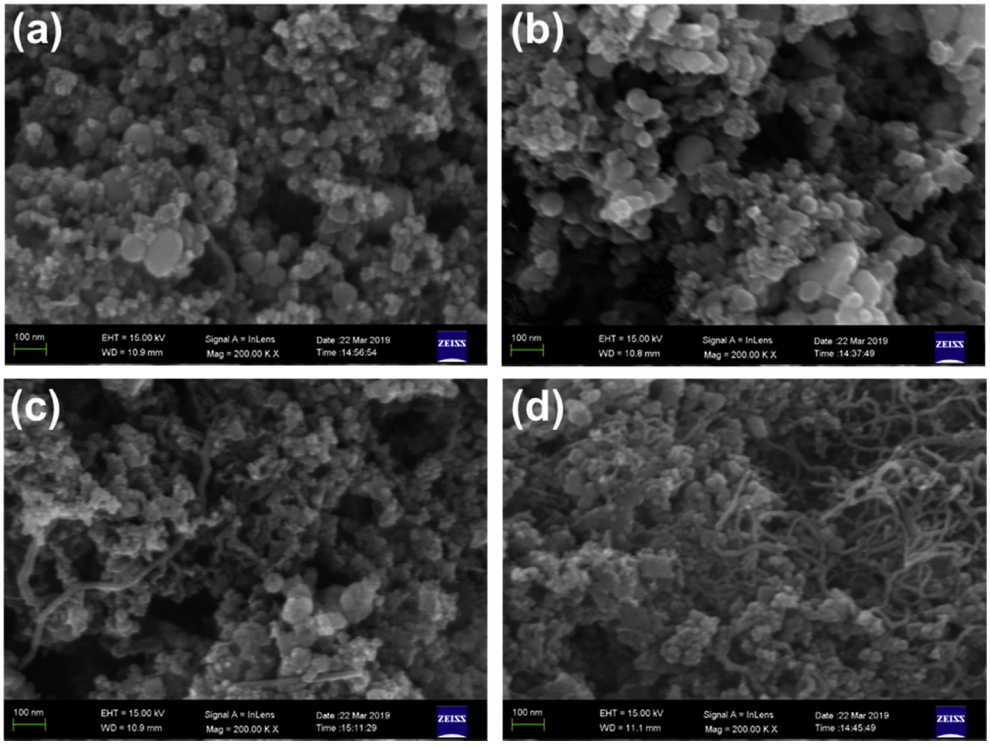

Fig. 4. SEM morphology of (a) Mn@C precursor, (b) MOC-200, (c) MOC-300, and (d) MOC-400 nanocomposites. SEM, scanning electron microscopy.

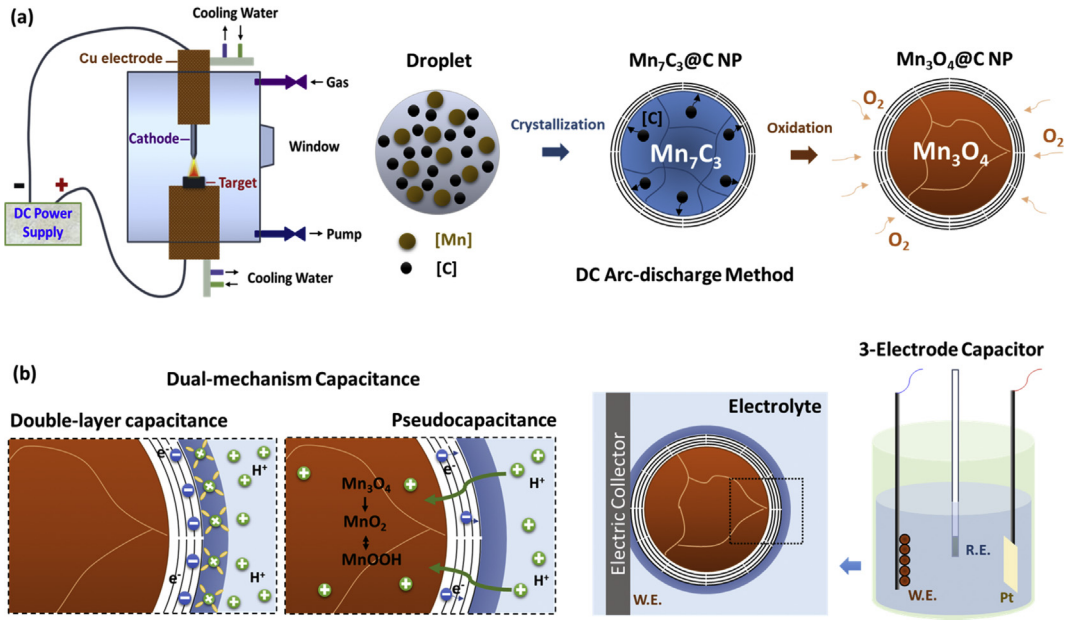

Fig. 5. Schematic illustration of (a) the formation mechanism for Mn@C and Mn_3O_4@C nanocomposites and (b) dual-mechanism capacitance (double-layer capacitance and pseudocapacitance) of Mn_3O_4@C with the core-shell nanostructure.

reducing the contact resistance. Another advantage is that it constrains the volume expansion of the core during cycling and protects it from dissolution in the electrolyte as well. Second, the faradaic redox pseudocapacitance involves the surface adsorption or intercalation of electrolyte cations ($C^+ = H^+$, Li^+, Na^+, and K^+) on the surface and in the bulk of electrode. In both charge-storage routes, redox reactions between the II, III, and IV oxidation states of Mn ions occur [6,51]. The synthesized Mn_3O_4 spinel structure is formed by interconnected tunnels and high volume of pores enabling the intercalation of protons and ions necessary for fast redox reactions, ensuring high pseudocapacitance and energy density [51]. Such a smart approach tailors the virtues of dual mechanisms, which will ensure high performance of the electrochemical supercapacitor.

With the purpose of comparing the capacitive properties of the as-synthesized Mn_3O_4@C nanocomposites, CV and galvanostatic charge-discharge tests are performed in KOH 30% w/w as the electrolyte, under a potential window of 0.8 V (−0.4 - 0.4 V), as illustrated in Fig. 6(a) and (b). According to the area of the loops in Fig. 6(a), the largest capacitance belongs to the MOC-200 sample, followed by MOC-300 and MOC-400 samples. Their shapes differ from the ideal rectangular shape of double-layer capacitors [16,52]; instead, two sharp anodic peaks with their corresponding cathodic pair are easily distinguished, which comes from the process of

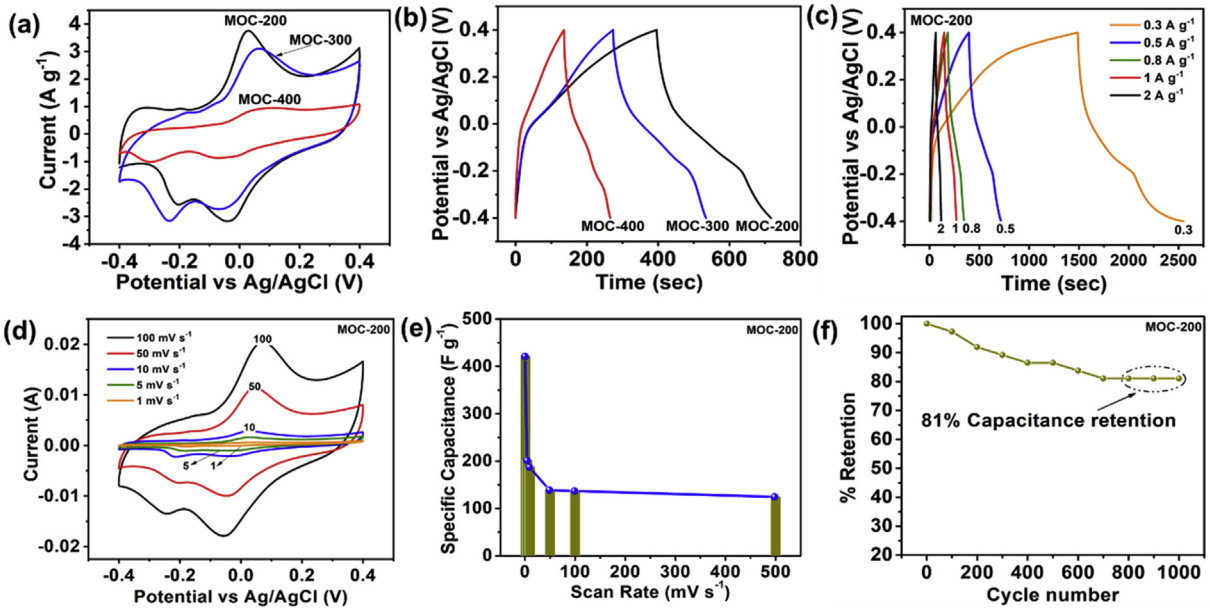

Fig. 6. (a) Cyclic voltammograms at scan rate of 10 mVs^{-1} in an aqueous solution of 30% w/w KOH, (b) Galvanostatic charge-discharge curves at 0.5 Ag^{-1} of MOC-200, MOC-300, and MOC-400 composite electrodes, (c) Galvanostatic charge-discharge curves at various current densities of MOC-200, (d) cyclic voltammetry curves at various scan rates of MOC-200, (e) specific capacitance vs. scan rate of MOC-200, (f) cycling stability at 100 mVs^{-1} of MOC-200.

intercalation/deintercalation of cations (K^+) and/or protons (H^+) from the electrolyte [53–55], due to the spinel 3D-interconnected tunnels arrangement of the pseudocapacitive material. Such an opened structure improves cation diffusion through the Mn_3O_4 microstructure [51,56]. The redox peaks reflect the redox transitions of Mn between different valence states (Mn^{+2}/Mn^{+3}, Mn^{+3}/Mn^{+4}) in an alkaline medium, including the following equations:

$$2(Mn_3O_4 \cdot 2H_2O) + 5OH^- \rightarrow 6MnO_2 \cdot 5H_2O + 3H^+ + 8e^- \quad (1)$$

$$MnO_2 \cdot 5H_2O + H^+ + e^- \rightleftarrows MnOOH + 5H_2O \quad (2)$$

where MnOOH indicates the interfacial manganese oxyhydroxide species under a higher oxidation state [27,57]. This behavior resembles the one from porous Mn_3O_4 nanocrystal–graphene electrodes [15], with the only difference that peaks are sharper in our work, which makes it reasonable that the type of carbon by our method plays a major role in the redox reactions. In other words, these cations and protons can be energetically attracted and wrapped within the defects and interlayer misalliances, boosting the pseudocapacitance feature reflected in the redox peaks pair around −0.25 V [23,24]. Efficient crystallization of the Mn_3O_4 core produced during annealing under air ambient is also a key factor for the peak enhancement during the ion exchange process [58]. As for the MOC-400 sample, an evident shift during cathodic and anodic processes could be originated from greatly reduced electric and ionic conductivity across the whole electrode interface due to the breakage of the carbon shell and the voids between the metal and carbon structures after oxidation, as shown above in Fig. 3(c) and (d') as well as in Fig. 4(d) and (d'). The maximum values of capacitance attained at 1 mVs^{-1} for MOC-200, MOC-300, and MOC-400 were 422, 213, and 136 Fg^{-1} (based on the total mass of carbon and Mn oxides), respectively. The CV results are confirmed by the galvanostatic curves shown in Fig. 6(b). The pseudocapacitive response is also evidenced in all the discharge curves through two potentials plateaus at −0.05 and −0.25 V. High electrochemical performance for MOC-200 nanocomposite can be ascribed to the enhanced interaction of well-defined core-shell structure, where open-layered and defect-enriched carbonaceous shells can deliver sufficient ions to the Mn_3O_4 core. Furthermore, the remaining manganese carbide helps decrease the contact resistance between Mn_3O_4 and the outer graphitic layer [27].

Charge-discharge results for MOC-200 are shown in detail in Fig. 6(c). The maximum value calculated from the curves is 401 Fg^{-1} (based on the total mass of carbon and Mn_3O_4), which corresponds to the current density of 0.3 Ag^{-1}. It is noticeable the decreasing tendency of capacitance when the scan rate or current density increases. The reason for this decrease is the electrolyte penetration in pores and defects of the carbon shell, thus the amount of ions is less available near the surface of the electrode. Moreover, the number of defects formed in the carbon shell during the oxidation process may have caused the mismatch among the layers. Once this misalliance is produced, the electronic and ionic conductivity will be attenuated, thus having great influence on the rate capability. Conversely, at low charge rates, electrolyte ions have time to diffuse into the depth of the pores, and the additional surface area is reached, which could be close to the full use of the electrode material, which can be confirmed in Fig. 6(d) and (e) [4,59]. These encouraging results are superior to previously reported capacitances: δ-MnO_2 nanofibers (380 Fg^{-1} at 5 mVs^{-1}) [47], doped Mn_3O_4 nanocrystals (272 Fg^{-1} at 0.5 Ag^{-1}) [60], Mn_3O_4-graphene oxide (276.5 Fg^{-1} at 0.4 Ag^{-1}) [48], Mn(MnO)eMn_5C_2-CNT (378.9 Fg^{-1} at 2 mVs^{-1}) [27], Mn_3O_4-graphene nanosheets (271.5 Fg^{-1} at 0.1 Ag^{-1}) [13], porous Mn_3O_4 nanocrystal-graphene (213.3 Fg^{-1} at 1 Ag^{-1}) [15], and multilevel porous graphite foam-Mn_3O_4 composite (260 Fg^{-1} at 1 mVs^{-1}) [61]. Furthermore, the stability of the MOC-200 composite is evaluated after 1000 cycles at 100 mVs^{-1} (Fig. 6(f)), demonstrating acceptable capacitance retention of 81%, which is ascribed to its exceptional structure arrangement. Here, we show the cyclability only until 1000 cycles due to the sudden drop in capacitance after 1200 cycles to 100 Fg^{-1}. The rapid descent in capacitance was caused by severe damage in the structure of the carbon shell. We presume that the volume change of the core was large enough to destroy the nanocomposite's cage. After the annealing process, the carbonaceous material underwent high tensile stress during the growing step as the core was oxidized, producing the increase of defects, which in consequence weakened the graphitic structure, affecting also its electronic conductivity. This will be confirmed in the next section.

HRTEM technique is used to study the microstructure change that occurs during the electrochemical process (Fig. 7) to clarify the reasons for the capacitance fading during cycling. Three distinctive images are found as the main representatives of the microstructure modifications. Fig. 7(a) shows those encapsulated nanoparticles, of which neither their core-shell structure nor their carbon layer has been altered. After the oxidation process of the precursor, the core of the nanoparticles decreased and the outer shell increased, as shown in Fig. 3(a'). Thus, the confinement effect by the enlarged shell alleviates the volume expansion during the continuous cycling, for these nanoparticles with the thickest carbonaceous shell for these nanoparticles. Fig. 7(b) represents the partially encapsulated nanoparticles. The failure is produced due to the

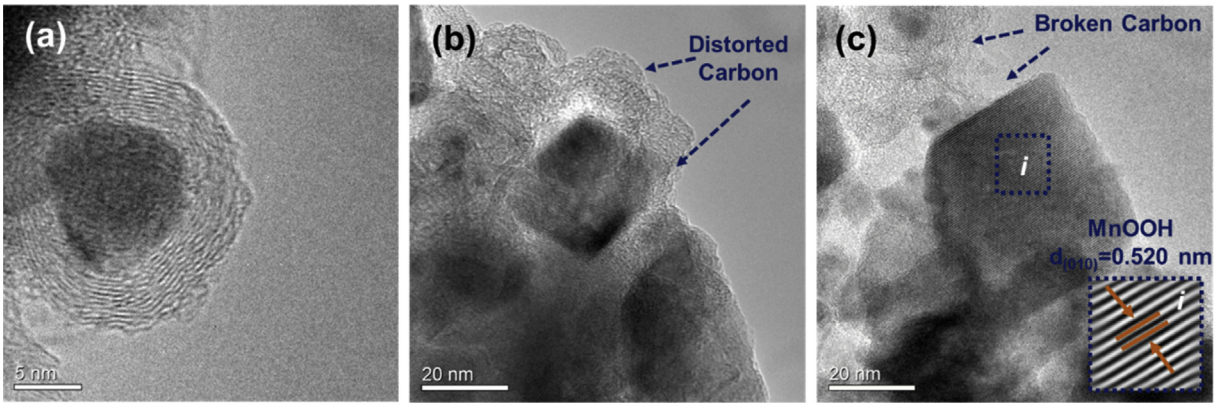

Fig. 7. TEM image of the nanoparticles in the MOC-200 electrode after 1000 cycles: (a) distinctive core/shell structure, (b) skewed carbon shell, and (c) bare nanoparticles. TEM, transmission electron microscopy.

insufficient protection of the less prominent carbon layers in comparison with the previous ones. Therefore, an obvious distortion of the shell is produced along with an increase in size and morphological change from spherical to rectangular. As for the bare nanoparticles (Fig. 7(c)), the size expansion and structural change of the in-core particle are much larger than the tolerance of the carbon shell. The average size of the nanoparticles before and after cycling was measured to be 30 nm and 41 nm, respectively. This represents a notable volume expansion and morphology modification whose deleterious effect was reflected on the cyclability of the electrode material. The lattice fringes on the particle are measured to be 0.52 nm, corresponding to (010) planes of MnOOH. It confirms that the degeneration of the electrochemical performance is aroused by the microstructure transformation from Mn_3O_4 to MnOOH. Furthermore, the produced MnOOH is not considered as an electroactive material for supercapacitors [62]. In other words, this material does not possess any pseudocapacitive behavior, which explains the decrease of capacitance throughout the stability test.

Further studies are being carried out to find a stable Mn_3O_4 crystal structure so that the formation of MnOOH is avoided. Lower oxidation temperature and longer annealing time are being tested to maintain the integrity of the graphitic layers. One of the most effective methods to achieve this is by doping the Mn_3O_4 nanoparticles with ions, i.e., Na^+ which has been done before by Li et al. [63] with V_2O_5. With the same concept, Liu et al. [64] synthetized an NCN^{-2}-doped MnO electrode material for Li-ion batteries and supercapacitors. In these two examples, the doped ion not only stabilized the structure but also improved the rate capability by promoting the mobility of ions from the electrolyte.

EIS measurements for MOC-200, MOC-300, and MOC-400 electrodes are performed to provide further evidence of the interfacial phenomena in Fig. 8(a). With this in mind, EIS was also tested for MOC-200 electrode before cycling and at the 1000th cycle (Fig. 8(b)) to deepen what is discussed in the electrochemical performance and TEM sections. The electrical equivalent circuit and the fitting the parameters for all the impedance spectra are shown in Fig. 8(c) and (d), where R1 and R2 correspond to the electrolyte resistance and charge transfer resistance or pseudocapacitive resistance. CPE1 and CPE2 are the constant phase elements for modeling the double-layer capacitance and pseudocapacitance, respectively. For a simplified circuit representation, a clear semicircle appears at high frequencies, and during low frequencies, a line with 45°-degree angle; however, in our case, the semicircle is depressed and the line appears between 90° and 45°. This can be associated with a non-uniform contact of the active material and the current collector across the electrode surface, which supports the usage of CPE1 and CPE2 [65]. W_1 accounts for the Warburg impedance during the dynamics of a diffusion-controlled process. It is embodied by a diagonal line with a slope of 45°. Diffusion can create an impedance known as the Warburg impedance. This impedance depends on the frequency of the potential perturbation. At high frequencies, the Warburg impedance is small because diffusing reactants do not have to move very far. At low frequencies, the reactants have to diffuse farther, thereby increasing the Warburg impedance.

When the impedance curve of MOC-200 composite is compared with that of its counterparts MOC-300 and MOC-400 (Fig. 8(a)), they corroborate the enhanced ion diffusion of the carbon constraint Mn_3O_4 nanoparticles. The charge transfer resistance values were calculated to be 2.9 and 3.2 Ω for MOC-300 and MOC-400, respectively, which are much higher than the one of MOC-200 (0.1 Ω). Once more, this is endorsed to the core-shell arrangement and the benefit of owning a carbon shell with superior conductivity,

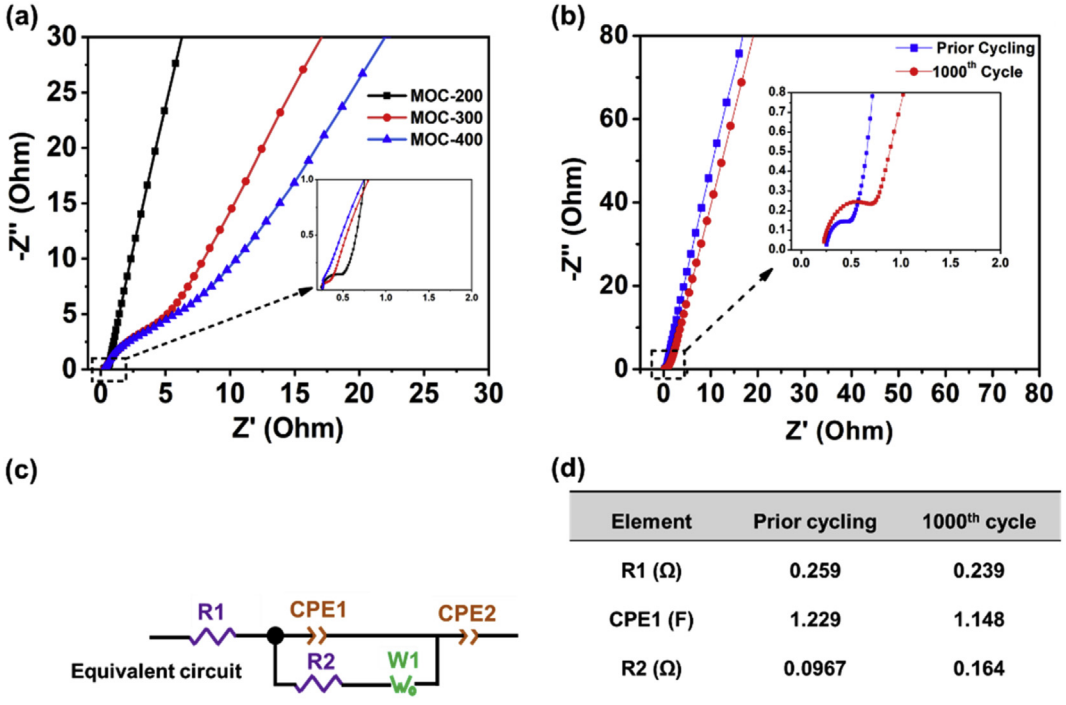

Element	Prior cycling	1000th cycle
R1 (Ω)	0.259	0.239
CPE1 (F)	1.229	1.148
R2 (Ω)	0.0967	0.164
W1 (Ω)	0.660	0.960
CPE2 (F)	1.485	0.954

Fig. 8. (a) Nyquist plots for MOC-200, MOC-300, and MOC-400 electrodes, (b) Nyquist plots for MOC-200 prior cycling and at the 1000th cycle, (c) the EIS electrical equivalent circuit, (d) fitting data for each impedance element of MOC-200 electrode prior cycling and at the 1000th cycle. The inset of (a) and (b) shows the magnified region of the Nyquist plot. EIS, electrochemical impedance spectroscopy.

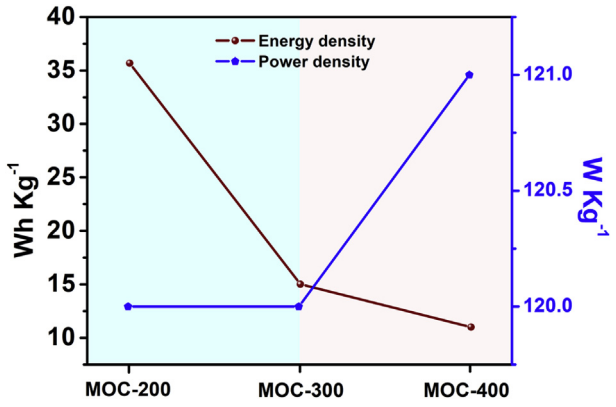

Fig. 9. Energy density and power density of the MOC-200, MOC-300, and MOC-400 composite electrodes calculated from the galvanostatic charge-discharge profiles at the current density of 0.3 Ag^{-1}.

matching the findings of electrochemical results. EIS results after cycling showed in the inset of Fig. 8(b) depict an enlargement of the depressed semicircle at high frequencies, which is related to the increment of the charge transfer limitation at electrode-electrolyte interface, and its diameter is equivalent to the Faradaic charge transfer resistance R2 [8,65]. After adequately fitting the data, the approximate values for R2 before cycling and at the 1000^{th} cycle are found to be 0.1 and 0.2 Ω, respectively. Small values of charge transfer resistance demonstrate the effectiveness of ion exchange. The capacitive decay is directly affected by the increased resistance, i.e., reduction of ion exchange within the electrode-electrolyte interface as displayed by the EIS results.

The applicability of the electrochemical supercapacitor depends on the relationship between two crucial factors: energy density and power density. The goal is to fulfill the requirements of high-energy storage matching with high power of delivery over a range of current densities. Thus, the performance of the samples is calculated at a current density of 0.3 Ag^{-1}, shown in Fig. 9.

Fig. 9 shows the electrode performance using the values of the capacitances from the charge-discharge tests, and this is why the power and energy density were not represented in a standard Ragone plot for full cell configurations such as asymmetric supercapacitors. MOC-200 owns the highest energy density of 36 $Whkg^{-1}$ and power density of 120 Wkg^{-1}. These values are superior in comparison with the EDLC-type supercapacitors [66,67] and even outperform MnO_2 supercapacitors [68], graphene-MnO_2, and graphene-Mn_3O_4 electrodes [7,69]. The performance ratifies the importance of the dual mechanism of the core-shell nanostructure, that is, pseudocapacitive Mn_3O_4 core encapsulated in a highly conductive graphitic shell.

Based on the results obtained previously, high electrochemical performance of the Mn_3O_4@C nanostructure can be ascribed to the carbon shell whose graphitization level plays an essential role in the intercalation-deintercalation of cations and protons from the electrolyte, the manganese carbide that enhances the overall conductivity, and the Mn_3O_4 core possessing high-energy storage of inherent pseudocapacitance.

4. Conclusions

In summary, Mn_3O_4@C nanocomposites have been synthesized using a facile, environmentally friendly, low-cost, and industry-oriented technique that combines the arc discharge method with a direct oxidation process. Microstructure analysis revealed that the sample retained a distinct core-shell structure after the annealing at 200 °C. The electrochemical results show high performance including excellent specific capacitance and remarkable capacitance retention. Dual-mechanism capacitance, i.e., the electric double-layer capacitance of the carbon shell and the pseudocapacitance from the Mn_3O_4 core, has been achieved simultaneously in the core-shell nanostructure, which can be a promising alternative for future high-performance supercapacitors.

Acknowledgments

The authors received support from the Fundamental Research Funds for the Central Universities (DUT17ZD101, DUT16LAB03), the Science and Technology Supported Plan (Industry Field) of Changzhou (CE20T160022), and the National Natural Science Foundation of China (51171033).

References

[1] P. Simon, Y. Gogotsi, Materials for electrochemical capacitors, Nat. Mater. 7 (2008) 845–854, https://doi.org/10.1038/nmat2297.
[2] B.E. Conway, V. Birss, J. Wojtowicz, The role and utilization of pseudocapacitance for energy storage by supercapacitors, J. Power Sources 66 (1997) 1–14, https://doi.org/10.1016/S0378-7753(96)02474-3.
[3] J. Li, X. Cheng, A. Shashurin, M. Keidar, Review of electrochemical capacitors based on carbon nanotubes and graphene, Graphene 01 (2012) 1–13, https://doi.org/10.4236/graphene.2012.11001.
[4] A.G. Pandolfo, A.F. Hollenkamp, Carbon properties and their role in supercapacitors, J. Power Sources 157 (2006) 11–27, https://doi.org/10.1016/j.jpowsour.2006.02.065.
[5] J. Sun, W. Li, B. Zhang, G. Li, L. Jiang, Z. Chen, R. Zou, J. Hu, 3D core/shell hierarchies of MnOOH ultrathin nanosheets grown on NiO nanosheet arrays for high-performance supercapacitors, Nanomater. Energy 4 (2014) 56–64, https://doi.org/10.1016/j.nanoen.2013.12.006.
[6] W. Wei, X. Cui, W. Chen, D.G. Ivey, Manganese oxide-based materials as electrochemical supercapacitor electrodes, Chem. Soc. Rev. 40 (2011) 1697–1721, https://doi.org/10.1039/c0cs00127a.
[7] G. Feng, Q. Jiangying, Z. Zongbin, Z. Quan, L. Beibei, Q. Jieshan, A green strategy for the synthesis of graphene supported Mn_3O_4 nanocomposites from graphitized coal and their supercapacitor application, Carbon 80 (2014) 640–650, https://doi.org/10.1016/j.carbon.2014.09.008.
[8] Y. Liu, W. Wang, Y. Wang, Y. Ying, L. Sun, X. Peng, Binder-free three-dimensional porous Mn_3O_4 nanorods/reduced graphene oxide paper-like electrodes for electrochemical energy storage, RSC Adv. 4 (2014) 16374, https://doi.org/10.1039/C4RA01395F.
[9] K. Subramani, D. Jeyakumar, M. Sathish, Manganese hexacyanoferrate derived Mn_3O_4 nanocubes-reduced graphene oxide nanocomposites and their charge storage characteristics in supercapacitors, Phys. Chem. Chem. Phys. 16 (2014) 4952–4961, https://doi.org/10.1039/c3cp54788d.
[10] B.G.S. Raj, R.N.R. Ramprasad, A.M. Asiri, J.J. Wu, S. Anandan, Ultrasound assisted synthesis of Mn_3O_4 nanoparticles anchored graphene nanosheets for supercapacitor applications, Electrochim. Acta 156 (2015) 127–137, https://doi.org/10.1016/j.electacta.2015.01.052.
[11] C. Liu, H. Song, C. Zhang, Y. Liu, C. Zhang, X. Nan, G. Cao, Coherent Mn_3O_4-carbon nanocomposites with enhanced energy-storage capacitance, Nano Res 8 (2015) 3372–3383, https://doi.org/10.1007/s12274-015-0837-4.
[12] Y. Fan, X. Zhang, Y. Liu, Q. Cai, J. Zhang, One-pot hydrothermal synthesis of Mn_3O_4/graphene nanocomposite for supercapacitors, Mater. Lett. 95 (2013) 153–156, https://doi.org/10.1016/j.matlet.2012.12.110.
[13] L. Zhu, S. Zhang, Y. Cui, H. Song, X. Chen, One step synthesis and capacitive performance of graphene nanosheets/Mn_3O_4 composite, Electrochim. Acta 89 (2013) 18–23, https://doi.org/10.1016/j.electacta.2012.10.157.
[14] B. Wang, J. Park, C. Wang, H. Ahn, G. Wang, Mn_3O_4 nanoparticles embedded into graphene nanosheets: preparation, characterization, and electrochemical properties for supercapacitors, Electrochim. Acta 55 (2010) 6812–6817, https://doi.org/10.1016/j.electacta.2010.05.086.
[15] D. Wang, Y. Li, Q. Wang, T. Wang, Facile synthesis of porous Mn_3O_4 nanocrystal-graphene nanocomposites for electrochemical supercapacitors, Eur. J. Inorg. Chem. 2012 (2012) 628–635, https://doi.org/10.1002/ejic.201100983.
[16] Y.F. Liu, G.H. Yuan, Z.H. Jiang, Z.P. Yao, Solvothermal synthesis of Mn_3O_4 nanoparticle/graphene sheet composites and their supercapacitive properties, J. Nanomater. 2014 (2014) 1–11.
[17] K.-S. Kim, S.-J. Park, Electrochemical performance of activated carbons/Mn_3O_4-carbon blacks for supercapacitor electrodes, Bull. Korean Chem. Soc. 34 (2013) 2343–2347, https://doi.org/10.5012/bkcs.2013.34.8.2343.
[18] W. Chen, Z. Fan, L. Gu, X. Bao, C. Wang, Enhanced capacitance of manganese oxide via confinement inside carbon nanotubes, Chem. Commun. 46 (2010) 3905–3907, https://doi.org/10.1039/c000517g.
[19] X. Liu, S.W. Or, C. Jin, Y. Lv, W. Li, C. Feng, F. Xiao, Y. Sun, Co_3O_4/C nanocapsules with onion-like carbon shells as anode material for lithium ion batteries,

Electrochim. Acta 100 (2013) 140–146, https://doi.org/10.1016/j.electacta.2013.03.179.
[20] X. Liu, S.W. Or, C. Jin, Y. Lv, W. Li, C. Feng, F. Xiao, Y. Sun, NiO/C nanocapsules with onion-like carbon shell as anode material for lithium ion batteries, Electrochim. Acta 100 (2013) 140–146, https://doi.org/10.1016/j.electacta.2013.03.179.
[21] X. Liu, N. Bi, C. Feng, S.W. Or, Y. Sun, C. Jin, W. Li, F. Xiao, Onion-like carbon coated CuO nanocapsules: a highly reversible anode material for lithium ion batteries, J. Alloy. Comp. 587 (2014) 1–5, https://doi.org/10.1016/j.jallcom.2013.10.178.
[22] J. Yu, J. Gao, F. Xue, X. Yu, H. Yu, X. Dong, H. Huang, A. Ding, X. Quan, G. Cao, Formation mechanism and optical characterization of polymorphic silicon nanostructures by DC arc-discharge, RSC Adv. 5 (2015) 68714–68721, https://doi.org/10.1039/C5RA11738K.
[23] G.F. Guo, H. Huang, F.H. Xue, C.J. Liu, H.T. Yu, X. Quan, X.L. Dong, Electrochemical hydrogen storage of the graphene sheets prepared by DC arc-discharge method, Surf. Coating. Technol. 228 (2013) 120–125, https://doi.org/10.1016/j.surfcoat.2012.07.016.
[24] X. Zhang, J. Guo, P. Guan, C. Liu, H. Huang, F. Xue, X. Dong, S.J. Pennycook, M.F. Chisholm, Catalytically active single-atom niobium in graphitic layers, Nat. Commun. 4 (2013) 1924, https://doi.org/10.1038/ncomms2929.
[25] C. Liu, H. Huang, G. Cao, F. Xue, R.A. Paredes Camacho, X. Dong, Enhanced electrochemical stability of Sn-carbon nanotube nanocapsules as lithium-ion battery anode, Electrochim. Acta 144 (2014) 376–382, https://doi.org/10.1016/j.electacta.2014.07.068.
[26] H. Huang, S. Gao, A.M. Wu, K. Cheng, X.N. Li, X.X. Gao, J.J. Zhao, X.L. Dong, G.Z. Cao, Fe_3N constrained inside C nanocages as an anode for Li-ion batteries through post-synthesis nitridation, Nanomater. Energy 31 (2017) 74–83, https://doi.org/10.1016/j.nanoen.2016.10.059.
[27] J. Zhang, J. Zang, Y. Wang, G. Xin, Y. Zhang, One-pot synthesis of a Mn(MnO)/Mn_5C_2/carbon nanotube nanocomposite for supercapacitors, RSC Adv. 4 (2014) 64162–64168, https://doi.org/10.1039/c4ra10940f.
[28] Y. Cao, Y. Xiao, Y. Gong, C. Wang, F. Li, One-pot synthesis of MnOOH nanorods on graphene for asymmetric supercapacitors, Electrochim. Acta 127 (2014) 200–207, https://doi.org/10.1016/j.electacta.2014.02.025.
[29] F. Yang, M. Zhao, Q. Sun, Y. Qiao, A novel hydrothermal synthesis and characterisation of porous Mn_3O_4 for supercapacitors with high rate capability, RSC Adv. 5 (2015) 9843–9847, https://doi.org/10.1039/C4RA10175H.
[30] Y. Ren, Q. Xu, J. Zhang, H. Yang, B. Wang, D. Yang, J. Hu, Z. Liu, Functionalization of biomass carbonaceous aerogels: selective preparation of MnO_2@CA composites for supercapacitors, ACS Appl. Mater. Interfaces 6 (2014) 9689–9697, https://doi.org/10.1021/am502035g.
[31] L.-B. Xing, S.-F. Hou, J. Zhou, S. Li, T. Zhu, Z. Li, W. Si, S. Zhuo, UV-assisted photoreduction of graphene oxide into hydrogels: high-rate capacitive performance in supercapacitor, J. Phys. Chem. C 118 (2014) 25924–25930, https://doi.org/10.1021/jp508682g.
[32] P. Asen, S. Shahrokhian, A high performance supercapacitor based on graphene/polypyrrole/Cu_2O–$Cu(OH)_2$ ternary nanocomposite coated on nickel foam, J. Phys. Chem. C 121 (2017) 6508–6519, https://doi.org/10.1021/acs.jpcc.7b00534.
[33] Y. Yamada, Y. Wang, N. Sasajima, Metal carbide-carbon peritectic systems as high-temperature fixed points in thermometry, Metrologia 43 (2006) L23–L27, https://doi.org/10.1088/0026-1394/43/5/N01.
[34] M. Naguib, O. Mashtalir, M.R. Lukatskaya, B. Dyatkin, C. Zhang, V. Presser, Y. Gogotsi, M.W. Barsoum, One-step synthesis of nanocrystalline transition metal oxides on thin sheets of disordered graphitic carbon by oxidation of MXenes, Chem. Commun. 50 (2014) 7420–7423, https://doi.org/10.1039/c4cc01646g.
[35] L.M. Malard, M.A. Pimenta, G. Dresselhaus, M.S. Dresselhaus, Raman spectroscopy in graphene, Phys. Rep. 473 (2009) 51–87, https://doi.org/10.1016/j.physrep.2009.02.003.
[36] A.C. Ferrari, Raman spectroscopy of graphene and graphite: disorder, electron-phonon coupling, doping and nonadiabatic effects, Solid State Commun. 143 (2007) 47–57, https://doi.org/10.1016/j.ssc.2007.03.052.
[37] Y. He, X. Han, Y. Du, B. Song, P. Xu, B. Zhang, Bifunctional nitrogen-doped microporous carbon microspheres derived from poly(o-methylaniline) for oxygen reduction and supercapacitors, ACS Appl. Mater. Interfaces 8 (2016) 3601–3608, https://doi.org/10.1021/acsami.5b07865.
[38] F. Tuinstra, J.L. Koenig, Raman spectrum of graphite, J. Chem. Phys. 53 (1970) 1126–1130, https://doi.org/10.1063/1.1674108.
[39] M.M. Lucchese, F. Stavale, E.H.M. Ferreira, C. Vilani, M.V.O. Moutinho, R.B. Capaz, C.A. Achete, A. Jorio, Quantifying ion-induced defects and Raman relaxation length in graphene, Carbon 48 (2010) 1592–1597, https://doi.org/10.1016/j.carbon.2009.12.057.
[40] M. Sevilla, A.B. Fuertes, Fabrication of porous carbon monoliths with a graphitic framework, Carbon 56 (2013) 155–166, https://doi.org/10.1016/j.carbon.2012.12.090.
[41] X. Liu, S. Or, S. Ho, C. Cheung, C. Leung, Z. Han, D. Geng, Z. Zhang, Full X-Ku band microwave absorption by Fe(Mn)/Mn_7C_3/C core/shell/shell structured nanocapsules, J. Alloy. Comp. 509 (2011) 9071–9075, https://doi.org/10.1016/j.jallcom.2011.06.031.
[42] S. Bag, K. Roy, C.S. Gopinath, C.R. Raj, Facile single-step synthesis of nitrogen-doped reduced graphene oxide-Mn_3O_4 hybrid functional material for the electrocatalytic reduction of oxygen, ACS Appl. Mater. Interfaces 6 (2014) 2692–2699, https://doi.org/10.1021/am405213z.
[43] M. Neumann, J. Wollschläger, C. Sanjeeviraja, A. Moses Ezhil Raj, V.B. Jothy, M. Jayachandran, M. Suendorf, S.G. Victoria, C. Ravidhas, XRD and XPS characterization of mixed valence Mn_3O_4 hausmannite thin films prepared by chemical spray pyrolysis technique, Appl. Surf. Sci. 256 (2009) 2920–2926, https://doi.org/10.1016/j.apsusc.2009.11.051.
[44] B. Murugan, A.V. Ramaswamy, D. Srinivas, C.S. Gopinath, V. Ramaswamy, Nature of manganese species in $Ce_{1-x}Mn_xO_{2-\delta}$ solid solutions synthesized by the solution combustion route, Chem. Mater. 17 (2005) 3983–3993, https://doi.org/10.1021/cm050401j.
[45] H. Xu, Z.-H. Liu, J. Zhang, Y. He, L. Kang, Z. Lei, F. Shi, X. Yang, Y. Bai, Mn_3O_4 nanocrystalline/graphene hybrid electrode with high capacitance, Electrochim. Acta 188 (2015) 398–405, https://doi.org/10.1016/j.electacta.2015.12.024.
[46] J. Sun, M. Zborowski, J.J. Chalmers, Quantification of both the presence, and oxidation state, of Mn in Bacillus atrophaeus spores and its imparting of magnetic susceptibility to the spores, Biotechnol. Bioeng. 108 (2011) 1119–1129, https://doi.org/10.1002/bit.23034.
[47] J.H. Lee, T.Y. Yang, H.Y. Kang, D.H. Nam, N.R. Kim, Y.Y. Lee, S.H. Lee, Y.C. Joo, Designing thermal and electrochemical oxidation processes for δ-MnO_2 nanofibers for high-performance electrochemical capacitors, J. Mater. Chem. A. 2 (2014) 7197–7204, https://doi.org/10.1039/c4ta00342j.
[48] L. Wang, Y. Li, Z. Han, L. Chen, B. Qian, X. Jiang, J. Pinto, G. Yang, Composite structure and properties of Mn_3O_4/graphene oxide and Mn_3O_4/graphene, J. Mater. Chem. A. 1 (2013) 8385–8397, https://doi.org/10.1039/c3ta10237h.
[49] M. Liu, J.M. Cowley, Encapsulation of manganese carbides within carbon nanotubes and nanoparticles, Carbon 33 (1995) 749–756, https://doi.org/10.1016/0008-6223(95)00014-5.
[50] B.E. Conway, Electrochemical Supercapacitors Scientific Fundamentals and Technological Applications, 1999, p. 736, https://doi.org/10.1007/978-1-4757-3058-6.
[51] O. Ghodbane, J.-L. Pascal, F. Favier, Microstructural effects on charge-storage properties in MnO_2 -based electrochemical supercapacitors, ACS Appl. Mater. Interfaces 1 (2009) 1130–1139, https://doi.org/10.1021/am900094e.
[52] D.T. Pham, T.H. Lee, D.H. Luong, F. Yao, A. Ghosh, V.T. Le, Carbon nanotube-bridged graphene 3D building blocks for ultrafast compact supercapacitors, ACS Nano (2015) 2018–2027.
[53] O. Ghodbane, F. Ataherian, N.L. Wu, F. Favier, In situ crystallographic investigations of charge storage mechanisms in MnO_2-based electrochemical capacitors, J. Power Sources 206 (2012) 454–462, https://doi.org/10.1016/j.jpowsour.2012.01.103.
[54] M.R. Lukatskaya, O. Mashtalir, C.E. Ren, Y. Dall'Agnese, P. Rozier, P.L. Taberna, M. Naguib, P. Simon, M.W. Barsoum, Y. Gogotsi, Cation intercalation and high volumetric capacitance of two-dimensional titanium carbide, Science 341 (2013) 1502–1505, https://doi.org/10.1126/science.1241488.
[55] M.D. Levi, M.R. Lukatskaya, S. Sigalov, M. Beidaghi, N. Shpigel, L. Daikhin, D. Aurbach, M.W. Barsoum, Y. Gogotsi, Solving the capacitive paradox of 2D MXene using electrochemical quartz-crystal admittance and in situ electronic conductance measurements, Adv. Energy Mater. 5 (2014), https://doi.org/10.1002/aenm.201400815, 1400815.
[56] T. Brousse, M. Toupin, R. Dugas, L. Athouël, O. Crosnier, D. Bélanger, Crystalline MnO_2 as possible alternatives to amorphous compounds in electrochemical supercapacitors, J. Electrochem. Soc. 153 (2006) A2171, https://doi.org/10.1149/1.2352197.
[57] B. Messaoudi, S. Joiret, M. Keddam, H. Takenouti, Anodic behaviour of manganese in alkaline medium, Electrochim. Acta 46 (2001) 2487–2498, https://doi.org/10.1016/S0013-4686(01)00449-2.
[58] L. Athouël, F. Moser, R. Dugas, O. Crosnier, D. Bélanger, T. Brousse, Variation of the MnO_2 birnessite structure upon charge/discharge in an electrochemical supercapacitor electrode in aqueous Na 2 SO 4 electrolyte, J. Phys. Chem. C 112 (2008) 7270–7277, https://doi.org/10.1021/jp0773029.
[59] D.P. Dubal, D.S. Dhawale, R.R. Salunkhe, C.D. Lokhande, A novel chemical synthesis of Mn_3O_4 thin film and its stepwise conversion into birnessite MnO_2 during super capacitive studies, J. Electroanal. Chem. 647 (2010) 60–65, https://doi.org/10.1016/j.jelechem.2010.05.010.
[60] R. Dong, Q. Ye, L. Kuang, X. Lu, Y. Zhang, X. Zhang, G. Tan, Y. Wen, F. Wang, Enhanced supercapacitor performance of Mn_3O_4 nanocrystals by doping transition-metal ions, ACS Appl. Mater. Interfaces 5 (2013) 9508–9516, https://doi.org/10.1021/am402257y.
[61] W. Li, X. Xu, C. Liu, M.C. Tekell, J. Ning, J. Guo, J. Zhang, D. Fan, Ultralight and binder-free all-solid-state flexible supercapacitors for powering wearable strain sensors, Adv. Funct. Mater. 27 (2017) 1–12, https://doi.org/10.1002/adfm.201702738.
[62] C. Hu, Y. Wu, K. Chang, Low-temperature hydrothermal synthesis of Mn_3O_4 and MnOOH single Crystals : determinant influence of oxidants, Chem. Mater. 20 (2008) 2890–2894.
[63] X. Li, C. Liu, C. Zhang, H. Fu, X. Nan, W. Ma, Z. Li, K. Wang, H. Wu, G. Cao, Effects of preinserted Na ions on Li-ion electrochemical intercalation properties of V_2O_5, ACS Appl. Mater. Interfaces 8 (2016) 24629–24637, https://doi.org/10.1021/acsami.6b08052.
[64] C. Liu, C. Zhang, H. Fu, X. Nan, G. Cao, Exploiting high-performance anode through tuning the character of chemical bonds for Li-ion batteries and capacitors, Adv. Energy Mater. 7 (2017), https://doi.org/10.1002/aenm.201601127.
[65] S. Devaraj, N. Munichandraiah, Electrochemical supercapacitor studies of nanostructured α-MnO_2 synthesized by microemulsion method and the effect of annealing, J. Electrochem. Soc. 154 (2007) A80, https://doi.org/10.1149/1.2404775.

[66] Y. Mun, C. Jo, T. Hyeon, J. Lee, K.-S. Ha, K.-W. Jun, S.-H. Lee, S.-W. Hong, H.I. Lee, S. Yoon, J. Lee, Simple synthesis of hierarchically structured partially graphitized carbon by emulsion/block-copolymer co-template method for high power supercapacitors, Carbon 64 (2013) 391–402, https://doi.org/10.1016/j.carbon.2013.07.092.

[67] M. Kaempgen, J. Ma, G. Gruner, G. Wee, S.G. Mhaisalkar, Bifunctional carbon nanotube networks for supercapacitors, Appl. Phys. Lett. 90 (2007) 2–3, https://doi.org/10.1063/1.2749187.

[68] H. Kim, B.N. Popov, Synthesis and characterization of MnO_2-based mixed oxides as supercapacitors, J. Electrochem. Soc. 150 (2003) D56–D62, https://doi.org/10.1149/1.1541675.

[69] Y. He, W. Chen, X. Li, Z. Zhang, J. Fu, C. Zhao, E. Xie, Freestanding three-dimensional graphene/MnO_2 composite networks as ultralight and flexible supercapacitor electrodes, ACS Nano 7 (2013) 174–182, https://doi.org/10.1021/nn304833s.